Inorganic Chemistry

pubs.acs.org/IC Article

Reversible Structural Transformation of Cu^{I}–Tb^{III} Heterometallic MOFs with Highly Efficient Detection Capability toward Penicillin

Ya-Qi Xue, Xintong Yang, Xiao-Long Sun, Zhang-Ye Han, Jianchao Sun, and Hongming He*

Cite This: *Inorg. Chem.* 2021, 60, 11081–11089 Read Online

ACCESS | Metrics & More | Article Recommendations | Supporting Information

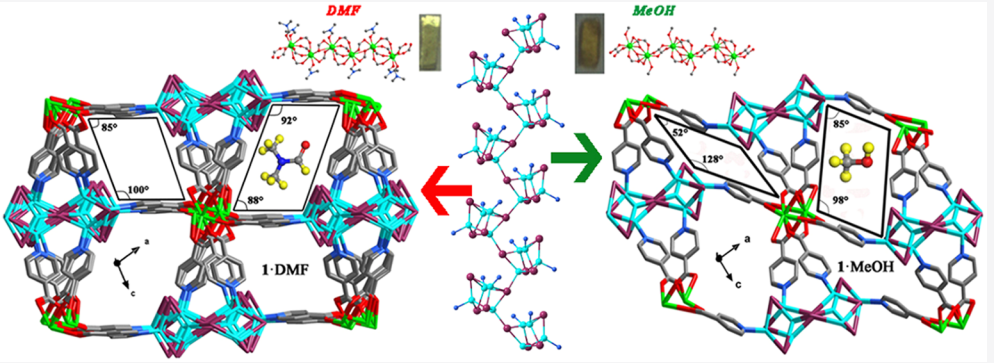

ABSTRACT: A Cu^{I}–Tb^{III} heterometallic MOF, namely **1**·DMF, was obtained via a coordination assembly process of isonicotinic acid with Cu^{I} and Tb^{III}. **1**·DMF can be switched to **1**·MeOH in methanol with a luminescent emission response. Meanwhile, **1**·MeOH exhibits a reversible single-crystal transformation to **1**·DMF after immersion in DMF. Both MOFs have superior physicochemical stability. The **1**·DMF-based biosensor has a remarkable sensing performance toward penicillin.

INTRODUCTION

Antibiotics as drugs and additives have been used in the treatment of multifarious bacterial infections.[1−3] Antibiotics also cause problems in terms of health and the environment due to the increasing antibiotic resistance of bacteria.[4] Up to now, some developed countries have taken measures to restrict the use of antibiotics in many fields. Particularly, penicillin triggers anaphylaxis for a specific population at only 1 ppb ($\sim 2.8 \times 10^{-9}$ M).[5] Detection technologies have been developed to monitor antibiotics, including fluorescence, mass spectrometry, and so on,[6−10] but some deficiencies significantly restrict their applications in the detection of antibiotics, such as time consumption, operational complexity, and high operating cost.

Aptamers are commonly used single-stranded RNA molecules with unique features, such as lack of immunogenicity, small size, good stability, and easy postmodification.[11] Also, they have three-dimensional (3D) constructions to recognize analytes.[12] By virtue of these outstanding features, aptamers can be used to build aptasensors to monitor analytes.[13,14] Significantly, electrochemical biosensors are of concern in food safety and environmental monitoring for the reasons of low operation cost, available portability, remarkable sensitivity, and exceptional selectivity.[15,16] In addition, diversified materials have been developed to amplify detection signals.[17−19] Metal−organic frameworks (MOFs) have been designed and used in many applications,[20−27] but their instability directly restricts the actual use of MOFs. Notably, heterometallic MOFs have attracted increasing interest in recent years, because such MOFs have plentiful structures, high stability, and fine photoelectric properties.[28−33] As we know, only a few reported MOFs have been developed to prepare aptasensors for electrochemical detection.[34−39] However, no heterometallic MOFs have been reported as electrochemical aptasensors to monitor penicillin.

Herein, we synthesized a Cu^{I}–Tb^{III} heterometallic MOF, namely **1**·DMF (DMF = *N*,*N*-dimethylformamide), based on isonicotinic acid (HINA) with a pyridine ring and a −COOH group. A reversible structural transformation of **1**·DMF occurs once it encounters MeOH to generate a different MOF, $\{[Tb_2(Cu_8I_8)(INA)_6(MeOH)_2]\cdot 6MeOH\}_n$ (namely **1**·MeOH), with a luminescent emission variation. Meanwhile, **1**·MeOH can quickly transform to **1**·DMF after immersion in DMF. The fabricated **1**·DMF-based biosensor can detect penicillin even in raw milk samples by an electrochemical impedance technique.

Received: March 27, 2021
Published: July 9, 2021

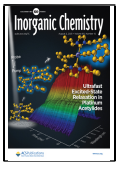

https://doi.org/10.1021/acs.inorgchem.1c00952
Inorg. Chem. 2021, 60, 11081−11089

EXPERIMENTAL SECTION

Materials and Methods. Chemicals were purchased and directly used in this work. The penicillin aptamer is 5′-NH_2-CTGAATTGG-ATCTCTCTTCTTGAGCGATCTCCACA-3′ from Shanghai Sangon Biotechnology.[40] Thermogravimetric analysis (TGA) was measured on a Shimadzu DTG-60A instrument. Fourier-transform infrared (FT-IR) spectra were obtained on a Bruker ALPHA-T FT-IR spectrometer. All experimental powder X-ray diffraction (PXRD) patterns were measured on a Rigaku D/max-2500 diffractometer. X-ray photoelectron spectroscopy (XPS) was carried out with an AXIS Ultra DLD X-ray photoelectron spectrometer. A Cary Eclipse fluorescence spectrophotometer was used to measure fluorescent spectra. Scanning electron microscope (SEM) images were obtained with a Nova Nano SEM 230 instrument. Elemental analyses were carried out with a PerkinElmer 240 instrument.

Preparation of $\{[(Cu_4I_4)_3Tb_3(INA)_9(DMF)_4]\cdot 3DMF\}_n$ (1·DMF). CuI (50 mg), $Tb(NO_3)_3\cdot 6H_2O$ (40 mg), 2-fluorobenzoic acid (80 mg), and HINA (40 mg) were ultrasonically dissolved in DMF (3 mL) and water (2 mL). The autoclave was sealed and heated at 100 °C for 24 h to obtain well-shaped crystals in a yield of 61%. Anal. Found: N, 5.14; H, 2.03; C, 20.51. FT-IR (cm^{-1}, Figure S1): 3426 (br), 3057 (br), 2934 (s), 2367 (s), 1656 (s), 1552 (s), 1498 (s), 1409 (s), 1238 (s), 1109 (s), 1061 (s), 1027 (s), 862 (s), 780 (s), 698 (s), 561(s), 439 (s).

Preparation of $\{[(Cu_8I_8)Tb_2(INA)_6(MeOH)_2]\cdot 6MeOH\}_n$ (1·MeOH). Crystals of 1·DMF were immersed in fresh MeOH for 2 days. Then well-shaped crystals were obtained in a yield of ∼100%. Anal. Found: N, 3.01; H, 1.92; C, 18.59. FT-IR (cm^{-1}, Figure S2): 3857 (m), 3754 (s), 2373 (s), 2339 (s), 1635 (s), 1587 (s), 1539 (s), 1402 (s), 1218 (s), 1061 (s), 1006 (s), 862 (s), 766 (s), 684 (s), 555 (s), 432 (s).

Single-Crystal X-ray Diffraction Determination and Refinement. 1·DMF and 1·MeOH measurements were both carried out on a SMARTAPEX II diffractometer (Mo Kα radiation). Absorption corrections were applied through a multiscan absorption correction. The absorption effects were implemented by using the SADABS program.[41] Their structures were accurately confirmed by a direct approach. All atoms except hydrogen were further processed through anisotropic refinement by SHELXL-2015 and OLEX2.[42−45] In addition, H atoms were added in the skeletons through a theoretical method. The deposited CCDC files are 1918830 for 1·DMF and 1918831 for 1·MeOH.

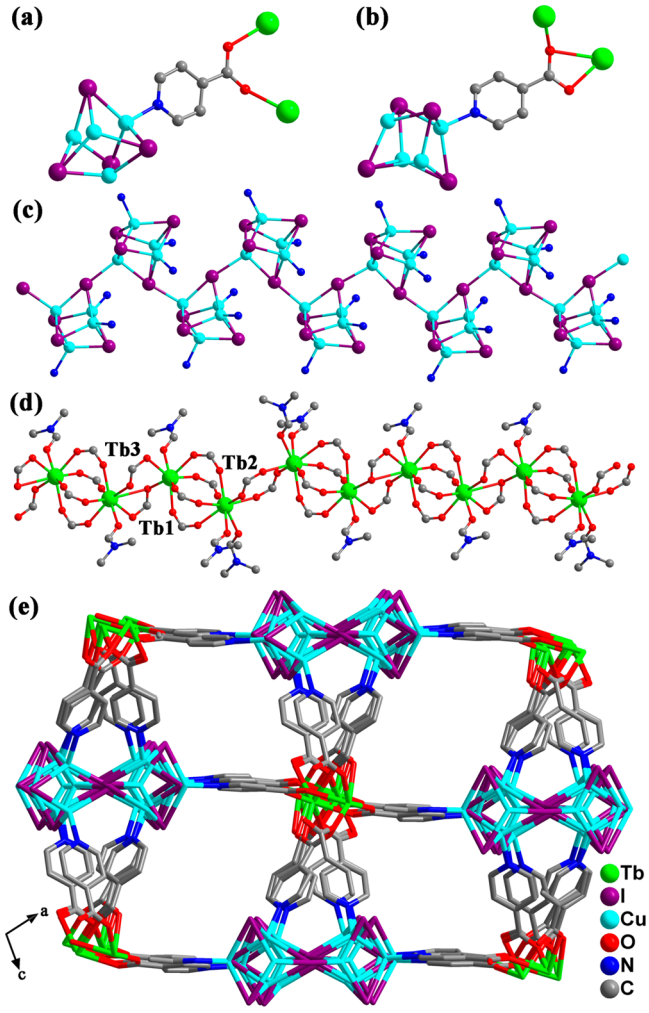

Figure 1. (a, b) Coordination modes of INA^-, (c, d) 1D Cu_4I_4- and Tb-based chains, and (e) the 3D porous structure after removal of coordinated and free guest molecules.

RESULTS AND DISCUSSION

Crystal Structure Analysis. 1·DMF crystallizes in the monoclinic system and $P2_1/n$ space group. The asymmetrical unit of 1·DMF contains 12 Cu^I, 3 Tb^{III}, 12 I^-, 9 INA^-, 4 coordinated DMF, and 1 free guest DMF (Figure S3). As shown in Figure 1a,b, two coordination modes of INA^- can be found in 1·DMF: μ_2-η^1:η^1 and μ_2-η^1:η^2. The Cu_4I_4 cluster is coordinated by the pyridine ring and two crystallographic Tb^{III} cations via $-COO^-$. As illustrated in Figure 1c, Cu_4I_4 clusters can generate one-dimensional (1D) chains. Three Cu^I ions in a Cu_4I_4 cluster coordinate with one N-donor in pyridine ring and three I^-; meanwhile, another Cu^I is coordinated with four I^- and served as a bridging site to connect different Cu_4I_4 clusters. Three crystallographic Tb^{III} cations exist in 1·DMF, including Tb1, Tb2, and Tb3, which are linked together via $-COO^-$ to form 1D chains (Figure 1d). Tb1 is coordinated with seven O atoms from six $-COO^-$ and a coordinated DMF. The coordination environment of Tb2 has eight O donors from six $-COO^-$ and two coordinated DMF molecules; meanwhile, Tb3 is connected with eight O-donors from six $-COO^-$ and one DMF. As shown in Figure 1e, Cu_4I_4- and Tb-based chains are linked together by INA^- linkers to form a 3D construction.

1·MeOH crystallizes in the monoclinic system with the $P2_1/n$ space group. It has one Tb^{III}, four Cu^I, four I^-, three fully deprotonated INA^- ligands, and one coordinated MeOH molecule (Figure S4). INA^- ligands show two coordination modes in 1·MeOH. Pyridine groups can coordinate with Cu_4I_4 clusters, but $-COO^-$ groups are able to connect with two crystallographic Tb^{III} cations by using the coordination modes μ_2-η^1:η^1 and μ_2-η^1:η^2 (Figures 2a,b). As displayed in Figure 2c, it exhibits a 1D Cu_4I_4 chain, which is similar to that in 1·DMF. However, the 1D Tb^{III}-based inorganic chain is significantly different from 1·DMF. As shown in Figure 2d, it is clearly found that all Tb^{III} cations adopt the coordination mode by connecting with seven O-donors from six $-COO^-$ and one coordinated MeOH. All Tb- and Cu_4I_4-based chains can be connected with each other by INA^- organic ligands to generate a 3D architecture, which is significantly different from that of 1·DMF (Figure 2e). Table 1 summarizes the crystal data.

PXRD and Stability Analysis of 1·DMF. The purity of 1·DMF was determined by a PXRD profile (Figure S5). More importantly, PXRD patterns of as-synthesized 1·DMF in air and water for different days at room temperature match very well with that of the as-synthesized 1·DMF (Figure S6), illustrating that 1·DMF has excellent stability under such conditions. In addition, the TGA curve of freshly as-synthesized 1·DMF shows a weight loss of about 4.96% at 170 °C due to the loss of guest DMF (calculated 5.02%)

https://doi.org/10.1021/acs.inorgchem.1c00952
Inorg. Chem. 2021, 60, 11081−11089

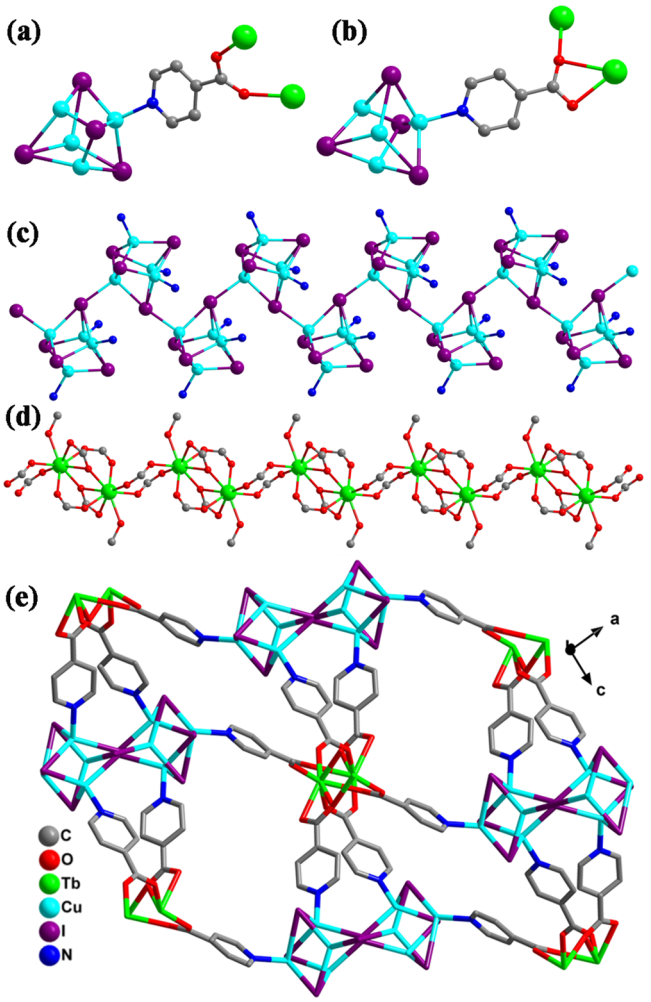

Figure 2. (a, b) Coordination modes of INA^-, (c, d) 1D Cu_4I_4- and Tb-based chains, and (e) the 3D porous construction after removal of coordinated and free guest molecules.

Table 1. Crystal Data of Both Samples

	1·DMF	1·MeOH
empirical formula	$C_{69}H_{71}O_{23}N_{14}I_{12}Cu_{12}Tb_3$	$C_{37}H_{27}O_{14}N_6I_8Cu_8Tb_2$
formula wt	4226.43	2621.00
cryst syst	monoclinic	monoclinic
space group	$P2_1/n$	$P2_1/n$
a (Å)	15.1510(8)	12.516(2)
b (Å)	25.2699(12)	8.3324(16)
c (Å)	28.9865(15)	31.140(6)
α (deg)	90	90
β (deg)	102.533(5)	94.673(3)
γ (deg)	90	90
V (Å^3)	10833.5(10)	3236.6(11)
Z	4	2
ρ_{calc} (g cm^{-3})	2.591	2.689
$F(000)$; R_{int}	7784; 0.0553	2378; 0.0676
N_{ref}	19086	5683
μ (mm^{-1})	7.716	8.595
GOF	0.943	1.096
R1 (reflections)	0.0429	0.0525
wR2 (reflections)	0.0757	0.1158

(Figure S7). The second weight loss is 6.87% at 320 °C, belonging to the coordinated DMF molecules (calculated 6.68%). The framework further decomposes with increasing temperature.

Structural Transformation. The as-synthesized 1·DMF was immersed in many organic solvents, including methanol, acetone, dichloromethane, toluene, petroleum ether, ether, ethanol, ethyl acetate, and acetonitrile, which were kept at room temperature for 2 days. The PXRD patterns of 1·DMF can be maintained in most organic solvents due to its high stability (Figure 3a). Nevertheless, the PXRD pattern of 1·DMF is obviously different in methanol, illustrating a single-crystal transformation can be caused by methanol to generate a new MOF (1·MeOH). As shown in Figure 3b, 1·MeOH and 1·DMF have evidently disparate channel shapes with different crystal colors becaise of the different coordination environments of Tb^{III}. Furthermore, we tried to directly prepare 1·MeOH by a solvothermal synthesis; nevertheless, 1·MeOH is not found under any synthetic conditions. Hence, 1·MeOH can only be generated by a methanol-induced structural transformation from 1·DMF.

The reversibility and conversion speed were investigated in detail. As shown in Figure 4a, some new diffraction peaks are found after immersing as-synthesized 1·DMF in MeOH for 30 min, which belongs to the diffraction peaks of 1·MeOH. The structural transformation from 1·DMF to 1·MeOH can proceed with increasing time in methanol, and the transformation is complete after 2 days. More importantly, 1·MeOH can rapidly transform to 1·DMF after immersion in DMF for only 30 s (Figure 4b). The transformation can be mainly attributed to solvent-induced Tb−O chain dissolution and reconstruction. As illustrated in Figure 4c, 1·DMF and 1·MeOH can convert to each other for at least 8 cycles, proving the excellent reversibility. No evident structural change was found in 1·DMF after it was soaked in DMF/MeOH (1/9 v/v) for 2 days. Simultaneously, 1·MeOH can maintain its skeleton structure in MeOH/DMF (1/9 v/v) for 30 s (Figure S8). The luminescent spectra of the transformation from 1·DMF to 1·MeOH at different immersion times were measured under an excitation at 330 nm. The maximum emission peak produces an obvious blue-shift phenomenon from 1·DMF to 1·MeOH (Figure 4d), which may be attributed to the more rigid structure in 1·MeOH in comparison to that in 1·DMF that significantly reduces the skeleton vibration and energy loss.[46]

Stability Analysis of 1·MeOH. To investigate the stability of 1·MeOH, it was immersed in frequently used organic solvents, such as acetone, dichloromethane, petroleum ether, toluene, ethanol, ethyl acetate, and acetonitrile, at room temperature for 2 days. As seen in Figure S9a, PXRD profiles are consistent with those of the matrix materials to prove a high stability in such solvents. More importantly, the water stability of MOFs is a vitally important factor in practical applications. The PXRD peaks of 1·MeOH in water for 2 days at room temperature are still consistent with the original pattern due to the excellent water stability (Figure S9b). PXRD patterns prove that 1·MeOH also has remarkable stability in air for 30 days.

Electrochemical Biosensing Performance. Cyclic voltammetry (CV) and electrochemical impedance spectroscopy (EIS) were used to study the electrochemical aptasensor at different stages in $[Fe(CN)_6]^{3-/4-}$ (0.5 mM) and KCl (0.1 M). As seen in Figure 5a, it is found that the bare Au electrode (AE) possesses remarkable redox peaks. 1·DMF-modified AE (1·DMF/AE) appreciably changes the redox peaks because of

https://doi.org/10.1021/acs.inorgchem.1c00952
Inorg. Chem. 2021, 60, 11081−11089

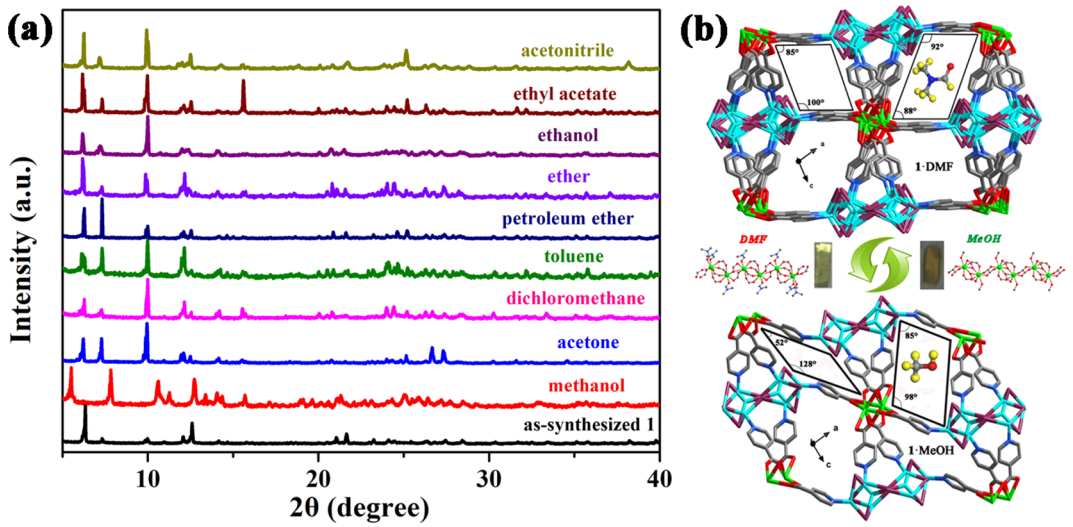

Figure 3. (a) PXRD data of **1**·DMF in organic solvents for 2 days at room temperature and (b) different shapes of channels and optical photos of **1**·DMF and **1**·MeOH.

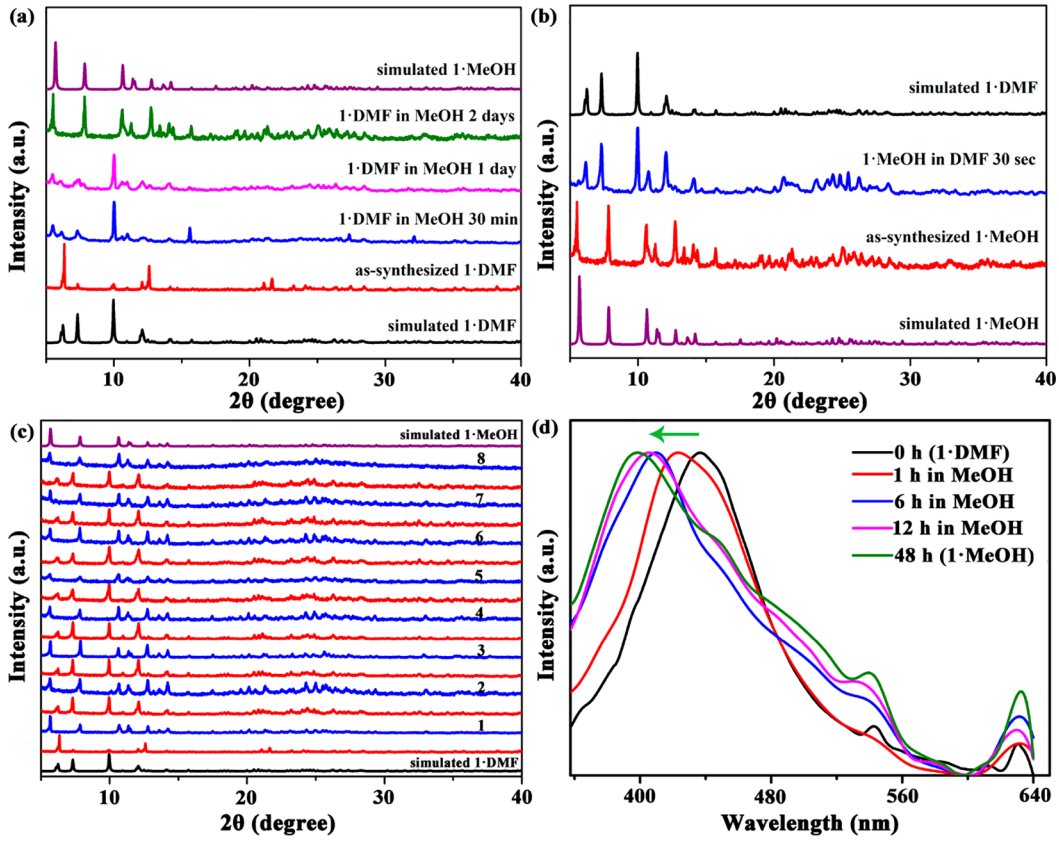

Figure 4. Switching speed of the structure transformation (a) from **1**·DMF to **1**·MeOH and (b) from **1**·MeOH to **1**·DMF, (c) the continuous reversibility between **1**·DMF and **1**·MeOH, and (d) the luminescent spectra of **1**·DMF in MeOH at different time intervals.

the relatively poor electrochemical property of INA^- ligands in **1**·DMF. This indicates that **1**·DMF is successfully coated on the bare AE. The apt/**1**·DMF/AE can be obtained after immersing **1**·DMF/AE in aptamer for 2 h with totally different CV curves. The fabricated penicillin/apt/**1**·DMF/AE also exhibits an obvious variation, illustrating the strong interaction between penicillin and the aptamer.

EIS measurements of different electrodes were performed to investigate the surface conditions at different modified stages. All Nyquist results were measured at open-circuit potential from 100 to 0.1 kHz. Figure 5b shows EIS plots at different stages. The equivalent circuit of simulated Nyquist curves is shown in Figure S10. There is a very small R_{ct} value of 0.18 kΩ for AE. The R_{ct} value of **1**·DMF/AE is 0.422 kΩ, which is significantly higher than that of AE to illustrate that **1**·DMF is on the surface of AE. Furthermore, the corresponding R_{ct} value of apt/**1**·DMF/AE rapidly soars to 0.567 kΩ because of the additional aptamer on the surface of **1**·DMF/AE to greatly

https://doi.org/10.1021/acs.inorgchem.1c00952
Inorg. Chem. 2021, 60, 11081−11089

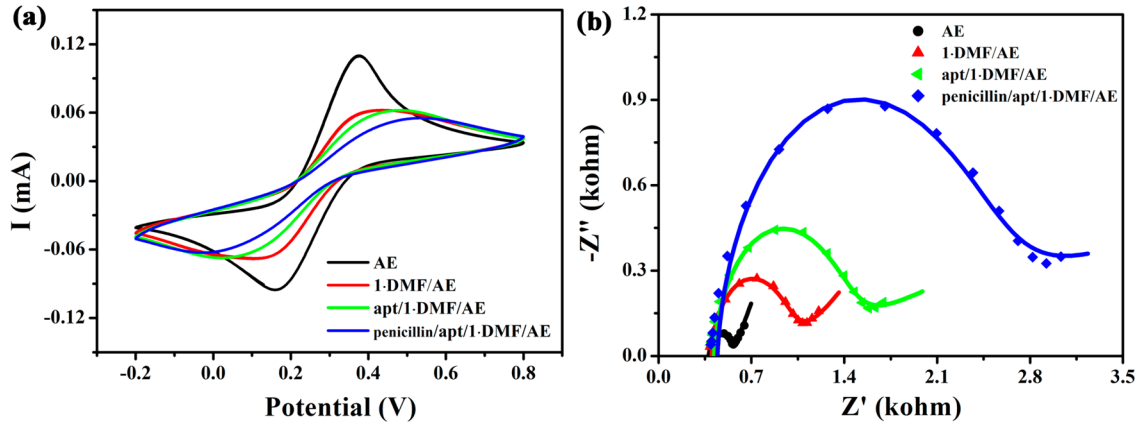

Figure 5. (a) CV curves and (b) EIS plots of AE, **1**·DMF/AE, atp/**1**·DMF/AE, and penicillin/atp/**1**·DMF/AE, respectively.

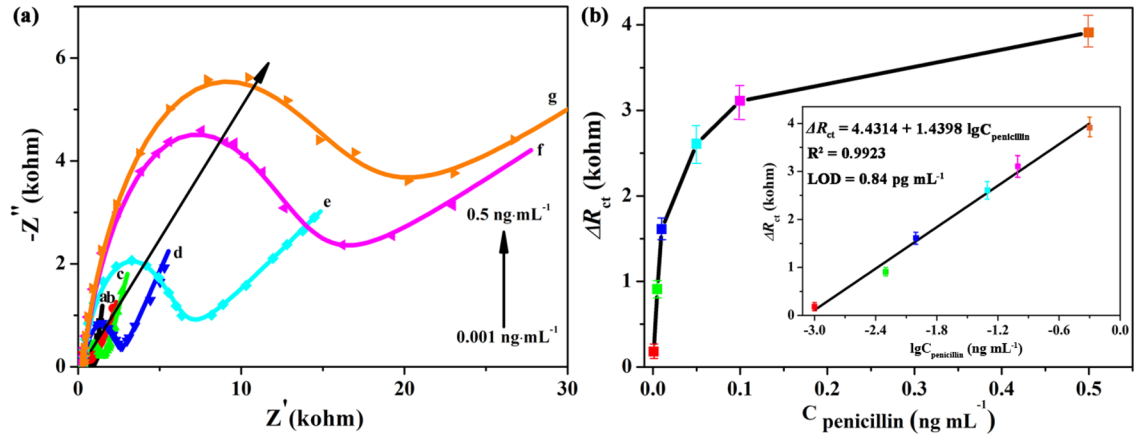

Figure 6. (a) EIS results and (b) the dependence of ΔR_{ct} on the penicillin concentration.

Table 2. Comparison of Penicillin Determinations

material	method	linear range (ng mL^{-1})	LOD (ng mL^{-1})	ref
Fe_3O_4 NPs and PEDOT-AuNPs composite	electrochemical aptasensor	0.1−200	0.057	49
methylene blue grafted polyurethane foam	flow injection analysis−solid-phase extraction	41−1200	12	50
hydroxylamine silver nanoparticle	surface-enhanced Raman spectroscopy	100−600	29	51
biohybrid magnetic particle	enzyme-linked immunosorbent assay		100	5
polymeric frit	nanoliquid chromatography		500	52
PenG-GlnBP-CF647	fluorescence polarization assay		0.356	53
1·DMF	electrochemical aptasensor	0.001−0.5	0.00084	this work

limit the electron transfer between AE and the electrode.[47] Meanwhile, the R_{ct} value of penicillin/apt/**1**·DMF/AE sharply increases to 0.79 kΩ in a penicillin solution (0.001 ng·mL^{-1}) due to the formation of penicillin/aptamer.[48] The PXRD pattern proves the integrated skeleton of **1**·DMF in penicillin/apt/**1**·DMF/AE (Figure S11). Additionally, the SEM image exhibits that deposited MOFs with small size can expose a large number of functional sites to immobilize aptamers (Figure S12).

Furthermore, a **1**·MeOH-based aptasensor was fabricated to detect penicillin under the same conditions. A similar electrochemical performance was observed (Figures S13 and S14). The R_{ct} value evidently increases after enhancing the modified layers on the surface of the AE. The immobilization efficiency and binding amount can be estimated by the R_{ct} variation value (ΔR_{ct}) calculated by the R_{ct} value before and after fabricating a new adsorbed layer. Figure S15 shows different ΔR_{ct} values of both MOF-based aptasensors. The **1**·DMF-based aptasensor has higher ΔR_{ct} values in comparison to those the of **1**·MeOH-based aptasensor, which exhibits that the higher binding amount of aptamers on the **1**·DMF-based aptasensor has a more sensitive detection performance. This encouraged us to investigate the sensing ability toward penicillin by using the **1**·DMF-based aptasensor.

apt/**1**·DMF/AE was incubated at different penicillin concentrations for 2 h to analyze the sensing ability. All Nyquist results of apt/**1**·DMF/AE are displayed in Figure 6. The R_{ct} value increases gradually in penicillin solutions from 0.001 to 0.5 ng mL^{-1}. The sensing performance may be ascribed to more penicillin on the surface of the electrode at a higher concentration. All ΔR_{ct} values at different penicillin concentrations are proportionally enhanced with the logarithm values of the penicillin concentration with the linear regression equation $\Delta R_{ct} = 4.4314 + 1.4398 \log C_{penicillin}$. The corresponding correlation coefficient (R^2) is 0.9923. The limit of detection (LOD) of the **1**·DMF-based aptasensor is

https://doi.org/10.1021/acs.inorgchem.1c00952
Inorg. Chem. 2021, 60, 11081−11089

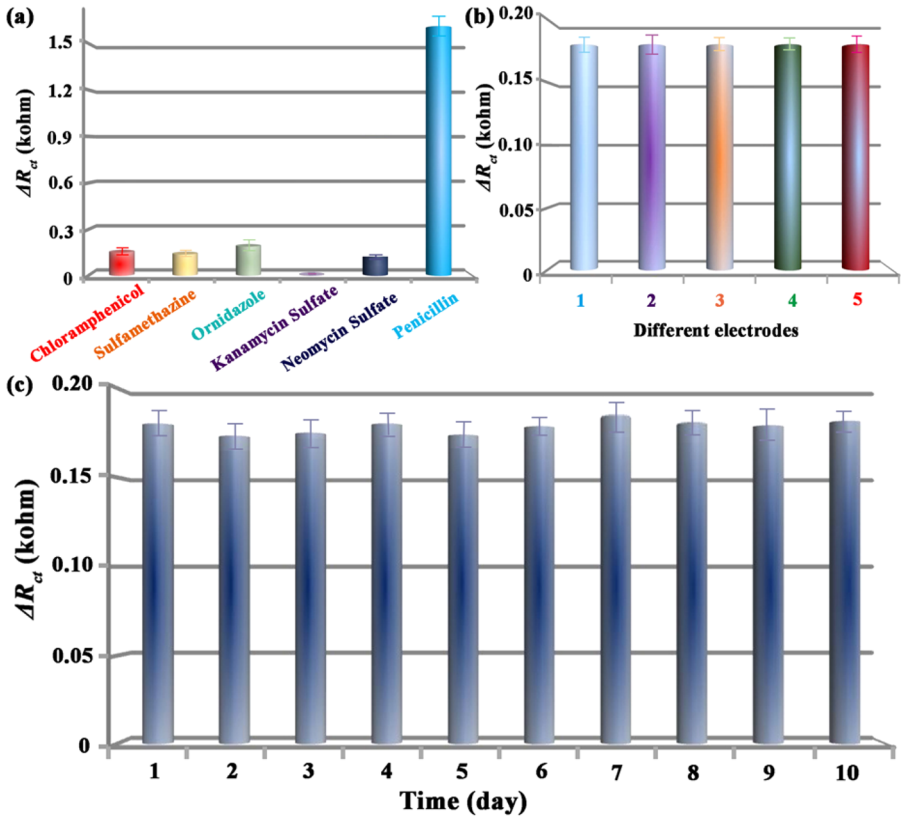

Figure 7. (a) Selectivity, (b) reproducibility, and (c) long-term stability of the developed **1**·DMF-based aptasensor.

0.84 pg mL^{-1}. As summarized in Table 2, the fabricated **1**·DMF-based aptasensor is superior to many reported sensors.

The selectivity of the fabricated **1**·DMF-based aptasensor can be investigated by comparing the ΔR_{ct} value in penicillin or other interfering antibiotics, including chloramphenicol, sulfamethazine, kanamycin sulfate, ornidazole, and neomycin sulfate. As displayed in Figure 7a, the fabricated **1**·DMF-based aptasensor shows a significant change after immersion in a penicillin solution at 0.01 ng mL^{-1}, but faint variations are found in interfering antibiotic solutions even at a 100-fold higher concentration (1 ng mL^{-1}) in comparison to that of penicillin. The result confirms that the obtained **1**·DMF-based aptasensor has exceptional selectivity to penicillin. Then the **1**·DMF-based aptasensor was measured in parallel by five different modified electrodes to detect penicillin at 0.001 ng mL^{-1}. The relative standard deviation (RSD) of these test electrodes is 3.51%, manifesting a remarkable producibility (Figure 7b). In addition, the same **1**·DMF-based biosensor was used continuously to detect penicillin (0.001 ng mL^{-1}) for 10 days. The ΔR_{ct} value is preserved very well in a refrigerator at −20 °C for 10 days to further illustrate the biosensor's operating stability and long-term storage (Figure 7c). In addition, −SH-modified aptamers were directly immobilized on AE (apt/AE). The preparation and sensing processes were virtually the same as those for the **1**·DMF-based electrochemical aptasensor without MOFs. Figure S16 shows that apt/AE has the same EIS Nyquist plots in the penicillin solution (0.001 ng mL^{-1}); meanwhile, EIS Nyquist plots of apt/AE only slightly increase in a penicillin solution at 0.05 ng mL^{-1}. Hence, the MOF is necessary for fabricating a highly sensitive electrochemical aptasensor.

The aptasensor based on **1**·DMF can monitor penicillin in real milk samples to estimate its practical capability, because penicillin, as a food additive, is broadly used to treat and feed cows, leading to penicillin residues in raw milk. It thus is remarkably meaningful to have a highly efficient detection of penicillin in real raw milk. The raw milk samples with different penicillin concentrations were investigated to confirm the accuracy by applying the standard addition approach. The test milk samples with penicillin concentrations at 0.001, 0.05, 0.1, and 0.5 ng mL^{-1} were manufactured by adding penicillin to the raw milk, respectively. Subsequently, EIS measurements were conducted for all of the above milk samples. The ΔR_{ct} value can be obtained to calculate the penicillin concentration (Table 3). The recovery of penicillin is in the range from

Table 3. Penicillin Determination in Raw Milk

spiked amount (ng mL^{-1})	ΔR_{ct} (Ω)	found amount (ng mL^{-1})	apparent recovery (%)	RSD (%)
0.001	190.4	0.001134	113.4	4.1
0.05	2593.2	0.05288	105.8	3.9
0.1	3038.0	0.1077	107.7	4.5
0.5	3999.8	0.5015	100.3	2.9

100.3% to 113.4%. In addition, all RSD values are significantly lower than 4.5%. Therefore, the **1**·DMF-based biosensor has an available practicality.

To understand the binding sites of aptamers on MOFs, the C 1s, Cu 2p, and Tb 4d high-resolution XPS spectra of MOF and apt/MOF were measured and analyzed in detail. As illustrated in Figure 8a, the C 1s signals of **1**·DMF and apt/**1**·DMF show an obvious difference in the range of 285.0−288.5 eV due to the adsorbed aptamers on the surface of **1**·DMF;

https://doi.org/10.1021/acs.inorgchem.1c00952
Inorg. Chem. 2021, 60, 11081−11089

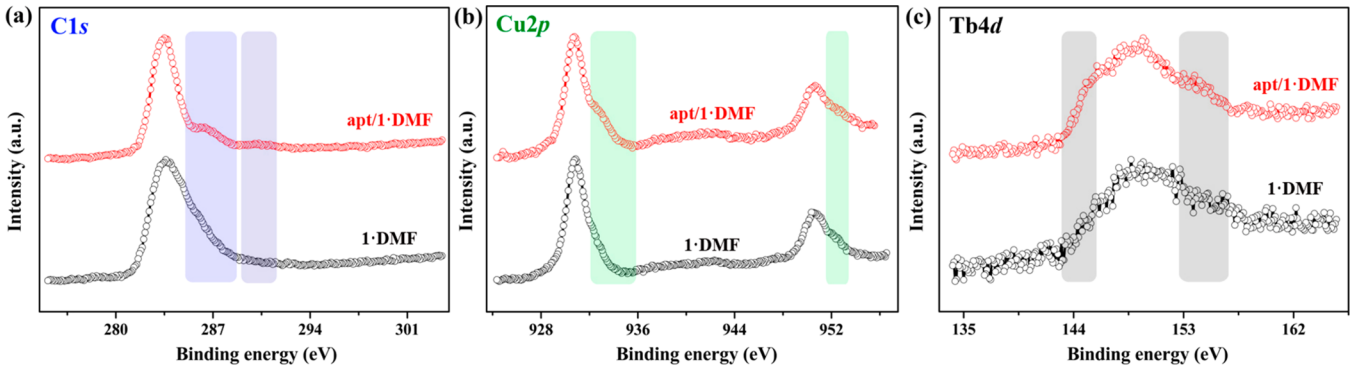

Figure 8. XPS spectra of C 1s (a), Cu 2p (b), and Tb 4d (c) of **1**·DMF (black) and apt/**1**·DMF (red).

meanwhile, a new weak XPS peak was observed at 290.5 eV via the $\pi\cdots\pi$ interaction between MOFs and aptamers.[54] In addition, the changes in the coordination environment of Cu and Tb in the MOF are shown in Figure 8b,c. In comparison with pure **1**·DMF, the Cu 2p core-level spectrum of apt/**1**·DMF exhibits two increasing peaks of 931.9−935.1 eV of Cu $2p_3$ and 951.8−954.8 eV of Cu $2p_1$, respectively. Similar to the Cu 2p XPS result, the high resolution Tb 4d XPS spectrum of apt/**1**·DMF displays two slightly enhanced parts around 143.3−146.4 and 152.3−157 eV ascribed to Tb−O and Tb $4d_5$, respectively. The apparent variation of C 1s, Cu 2p, and Tb 4d XPS spectra can confirm that aptamers are covered on the MOF via the $\pi\cdots\pi$ force between the organic ligands and the bases in aptamers and the coordination interaction of aptamers and metal sites (Cu or Tb) in MOFs.

CONCLUSION

In summary, we successfully exploited and prepared Cu^{I}−Tb^{III} heterometallic MOFs, which can fabricate portable and useful electrochemical biosensors for detecting penicillin with splendid selectivity and excellent sensitivity. The LOD is 0.84 pg mL^{-1}; meanwhile, the **1**·DMF-based aptasensor can accurately monitor penicillin in raw milk. Interestingly, a reversible solvent-induced structural transformation can be found between **1**·DMF and **1**·MeOH after immersion in MeOH or DMF.

ASSOCIATED CONTENT

Supporting Information

The Supporting Information is available free of charge at https://pubs.acs.org/doi/10.1021/acs.inorgchem.1c00952.

Asymmetric unit, TGA, PXRD, FT-IR spectra, and additional experimental procedures (PDF)

Accession Codes

CCDC 1918830−1918831 contain the supplementary crystallographic data for this paper. These data can be obtained free of charge via www.ccdc.cam.ac.uk/data_request/cif, or by emailing data_request@ccdc.cam.ac.uk, or by contacting The Cambridge Crystallographic Data Centre, 12 Union Road, Cambridge CB2 1EZ, UK; fax: +44 1223 336033.

AUTHOR INFORMATION

Corresponding Author

Hongming He − *Tianjin Key Laboratory of Structure and Performance for Functional Molecules, College of Chemistry, Tianjin Normal University, Tianjin 300387, People's Republic of China;* orcid.org/0000-0001-5535-8825; Email: hehongminghz@163.com, hxxyhhm@tjnu.edu.cn

Authors

Ya-Qi Xue − *Tianjin Key Laboratory of Structure and Performance for Functional Molecules, College of Chemistry, Tianjin Normal University, Tianjin 300387, People's Republic of China*

Xintong Yang − *Tianjin Key Laboratory of Structure and Performance for Functional Molecules, College of Chemistry, Tianjin Normal University, Tianjin 300387, People's Republic of China*

Xiao-Long Sun − *Tianjin Key Laboratory of Structure and Performance for Functional Molecules, College of Chemistry, Tianjin Normal University, Tianjin 300387, People's Republic of China*

Zhang-Ye Han − *Tianjin Key Laboratory of Structure and Performance for Functional Molecules, College of Chemistry, Tianjin Normal University, Tianjin 300387, People's Republic of China*

Jianchao Sun − *School of Environment and Material Engineering, Yantai University, Yantai, Shandong 264005, People's Republic of China;* orcid.org/0000-0003-2051-6365

Complete contact information is available at: https://pubs.acs.org/10.1021/acs.inorgchem.1c00952

Notes

The authors declare no competing financial interest.

ACKNOWLEDGMENTS

This research was supported by the National Natural Science Foundation of China (21801187) and the Opening Project of Key Laboratory of Polyoxometalate and Reticular Material Chemistry of Ministry of Education.

REFERENCES

(1) Blaskovich, M. A. T.; Zuegg, J.; Elliott, A. G.; Cooper, M. A. Helping Chemists Discover New Antibiotics. *ACS Infect. Dis.* **2015**, *1*, 285−287.

(2) Zhou, X.; Wang, J.; Lu, C.; Liao, Q.; Gudda, F. O.; Ling, W. Antibiotics in Animal Manure and Manure-Based Fertilizers: Occurrence and Ecological Risk Assessment. *Chemosphere* **2020**, *255*, 127006.

(3) Huang, K.; Chen, J.; Guan, M.; Xia, H.; Lin, L. Effects of Biochars on the Fate of Antibiotics and Their Resistance Genes During Vermicomposting of Dewatered Sludge. *J. Hazard. Mater.* **2020**, *397*, 122767.

(4) Chait, R.; Craney, A.; Kishony, R. Antibiotics Interactions that Select Against Resistance. *Nature* **2007**, *446*, 668−671.
(5) Broto, M.; Matas, S.; Babington, R.; Marco, M.-P.; Galve, R. Immunochemical Detection of Penicillins by Using Biohybrid Magnetic Particles. *Food Control* **2015**, *51*, 381−389.
(6) Xie, Y.; Zhu, X.; Sun, Y.; Wang, H.; Qian, H.; Yao, W. Rapid Detection Method for Nitrofuran Antibiotic Residues by Surface-Enhanced Raman Spectroscopy. *Eur. Food Res. Technol.* **2012**, *235*, 555−561.
(7) Wu, Y.; Tang, L.; Huang, L.; Han, Z.; Wang, J.; Pan, H. A Low Detection Limit Penicillin Biosensor Based on Single Graphene Nanosheets Preadsorbed with Hematein/Ionic Liquids/Penicillinase. *Mater. Sci. Eng., C* **2014**, *39*, 92−99.
(8) Jadhav, M. R.; Pudale, A.; Raut, P.; Utture, S.; Shabeer, T. P. A.; Banerjee, K. A Unified Approach for High-Throughput Quantitative Analysis of the Residues of Multi-Class Veterinary Drugs and Pesticides in Bovine Milk using LC-MS/MS and GC−MS/MS. *Food Chem.* **2019**, *272*, 292.
(9) Kantiani, L.; Farré, M.; Barceló, D.; Barceló, D. Analytical Methodologies for the Detection of β-Lactam Antibiotics in Milk and Feed Samples. *TrAC, Trends Anal. Chem.* **2009**, *28*, 729−744.
(10) Jalili, R.; Khataee, A.; Rashidi, M. R.; Razmjou, A. Detection of Penicillin G Residues in Milk Based on Dual-Emission Carbon Dots and Molecularly Imprinted Polymers. *Food Chem.* **2020**, *314*, 126172.
(11) Narayan, C.; Kwon, J.; Kim, C.; Kim, S. J.; Jang, S. K. Virus-Based SELEX (Viro-SELEX) Allows Development of Aptamers Targeting Knotty Proteins. *Analyst* **2020**, *145*, 1473−1482.
(12) Zhu, Q.-Q.; Zhang, W.-W.; Zhang, H.-W.; Yuan, R.; He, H. Elaborately Manufacturing an Electrochemical Aptasensor Based on Gold Nanoparticle/COF Composites for Amplified Detection Performance. *J. Mater. Chem. C* **2020**, *8*, 16984−16991.
(13) Yuan, R.; He, H. Construction of an Electrochemical Aptasensor Based on a Carbazole-Bearing Porous Organic Polymer for Rapid and Ultrasensitive Detection of Penicillin. *Appl. Surf. Sci.* **2021**, *563*, 150307.
(14) Zhao, Y.; Gosai, A.; Shrotriya, P. Effect of Receptor Attachment on Sensitivity of Label Free Microcantilever Based Biosensor using Malachite Green Aptamer. *Sens. Actuators, B* **2019**, *300*, 126963.
(15) Murphy, M.; Theyagarajan, K.; Prabusankar, G.; Senthilkumar, S.; Thenmozhi, K. Electrochemical Biosensor for the Detection of Hydrogen Peroxide using Cytochrome C Covalently Immobilized on Carboxyl Functionalized Ionic Liquid/Multiwalled Carbon Nanotube Hybrid. *Appl. Surf. Sci.* **2019**, *492*, 718−725.
(16) Dong, H.; Zhang, L.; Liu, W.; Tian, Y. Label-Free Electrochemical Biosensor for Monitoring of Chloride Ion in an Animal Model of Alzhemier's Disease. *ACS Chem. Neurosci.* **2017**, *8*, 339−346.
(17) Reta, N.; Saint, C. P.; Michelmore, A.; Prieto-Simon, B.; Voelcker, N. H. Nanostructured Electrochemical Biosensors for Label-Free Detection of Water- and Food-Borne Pathogens. *ACS Appl. Mater. Interfaces* **2018**, *10*, 6055−6072.
(18) Xu, Z.; Han, R.; Liu, N.; Gao, F.; Luo, X. Electrochemical Biosensors for the Detection of Carcinoembryonic Antigen with Low Fouling and High Sensitivity Based on Copolymerized Polydopamine and Zwitterionic Polymer. *Sens. Actuators, B* **2020**, *319*, 128253.
(19) Zou, J.; Mao, D.; Wee, A. T. S.; Jiang, J. Micro/Nano-Structured Ultrathin g-C_3N_4/Ag Nanoparticle Hybrids as Efficient Electrochemical Biosensors for L-Tyrosine. *Appl. Surf. Sci.* **2019**, *467*, 608−618.
(20) He, H.; Perman, J. A.; Zhu, G.; Ma, S. Metal−Organic Frameworks for CO_2 Chemical Transformations. *Small* **2016**, *12*, 6309−6324.
(21) Yuan, Y.; He, H. State of the Art Methods and Challenges of Luminescent Metal−Organic Frameworks for Antibiotic Detection. *Inorg. Chem. Front.* **2020**, *7*, 4293−4319.
(22) Ma, Y.-J.; Hu, J.-X.; Han, S.-D.; Pan, J.; Li, J.-H.; Wang, G.-M. Manipulating On/Off Single-Molecule Magnet Behavior in a Dy(III)-Based Photochromic Complex. *J. Am. Chem. Soc.* **2020**, *142*, 2682−2689.
(23) Jiang, X.-F.; Han, S.-D.; Wang, A.-N.; Pan, J.; Wang, G.-M. The Tri(imidazole)-Derivative Moiety: A New Category of Electron Acceptors for the Design of Crystalline Hybrid Photochromic Materials. *Chem. - Eur. J.* **2021**, *27*, 1410−1415.
(24) He, H.; Sun, Q.; Gao, W.; Perman, J. A.; Sun, F.; Zhu, G.; Aguila, B.; Forrest, K.; Space, B.; Ma, S. A Stable Metal−Organic Framework Featuring Local Buffer Environment for Carbon Dioxide Fixation. *Angew. Chem., Int. Ed.* **2018**, *57*, 4657−4662.
(25) Zhu, L.; Wong, B. J. C.; Li, Y.; Xin, H.; Liu, B.; Lei, J. Metal−Organic Framework for Profiling of Subcellular Glutathione. *Chem. - Eur. J.* **2019**, *25*, 4665−4669.
(26) Zhou, J.; Li, Y.; Wang, W.; Tan, X.; Lu, Z.; Han, H. Metal−Organic Frameworks-Based Sensitive Electrochemiluminescence Biosensing. *Biosens. Bioelectron.* **2020**, *164*, 112332.
(27) Hatamluyi, B.; Rezayi, M.; Beheshti, H. R.; Boroushaki, N. T. Ultra-Sensitive Molecularly Imprinted Electrochemical Sensor for Patulin Detection Based on a Novel Assembling Strategy using Au@Cu-MOF/N-GQDs. *Sens. Actuators, B* **2020**, *318*, 128219.
(28) Liu, J.-H.; Gu, Y.-N.; Chen, Y.; Qi, Y.-J.; Li, X.-X.; Zheng, S.-T. Incorporating Cuprous-Halide Clusters and Lanthanide Clusters to Construct Heterometallic Cluster Organic Frameworks with Luminescence and Gas Adsorption Properties. *CrystEngComm* **2018**, *20*, 738−745.
(29) Liu, J.-H.; Qi, Y.-J.; Zhao, D.; Li, H.-H.; Zheng, S.-T. Heterometallic Organic Frameworks Built from Trinuclear Indium and Cuprous Halide Clusters: Ligand-Oriented Assemblies and Iodine Adsorption Behavior. *Inorg. Chem.* **2019**, *58*, 516−523.
(30) Lin, L.-D.; Ge, R.; Zhang, J.; Li, Z.; Yu, H.; Liu, J.-H.; Li, X.-X.; Sun, Y.-Q.; Zhao, D.; Zheng, S.-T. Construction of Two High−Nuclear 3d−4d Heterometallic Cluster Organic Frameworks by Introducing a Bifunctional Tripodal Alcohol as a Structure−Directing Agent. *Chem. - Asian J.* **2019**, *14*, 1985−1991.
(31) Wang, D.; Liu, Z.; Xu, L.; Li, C.; Zhao, D.; Ge, G.; Wang, Z.; Lin, J. A Heterometallic Metal−Organic Framework Based on Multi-Nuclear Clusters Exhibiting High Stability and Selective Gas Adsorption. *Dalton Trans.* **2019**, *48*, 278−284.
(32) Skorupskii, G.; Dincă, M. Electrical Conductivity in a Porous, Cubic Rare-Earth Catecholate. *J. Am. Chem. Soc.* **2020**, *142*, 6920−6924.
(33) Sheberla, D.; Bachman, J. C.; Elias, J. S.; Sun, C. J.; Shao-Horn, Y.; Dincă, M. Conductive MOF Electrodes for Stable Supercapacitors with High Areal Capacitance. *Nat. Mater.* **2017**, *16*, 220−224.
(34) Liu, C.-S.; Sun, C.-X.; Tian, J.-Y.; Wang, Z.-W.; Ji, H.-F.; Song, Y.; Zhang, S.; Zhang, Z.-H.; He, L.-H.; Du, M. Highly Stable Aluminum-based Metal−Organic Frameworks as Biosensing Platforms for Assessment of Food Safety. *Biosens. Bioelectron.* **2017**, *91*, 804−810.
(35) Su, F.; Zhang, S.; Ji, H.; Zhao, H.; Tian, J.-Y.; Liu, C.-S.; Zhang, Z.; Fang, S.; Zhu, X.; Du, M. Two-Dimensional Zirconium-Based Metal−Organic Framework Nanosheet Composites Embedded with Au Nanoclusters: A Highly Sensitive Electrochemical Aptasensor toward Detecting Cocaine. *ACS Sens* **2017**, *2*, 998−1005.
(36) He, L.; Duan, F.; Song, Y.; Guo, C.; Zhao, H.; Tian, J.-Y.; Zhang, Z.; Liu, C.-S.; Zhang, X.; Wang, P.; Du, M.; Fang, S.-M. 2D Zirconium-based Metal−Organic Framework Nanosheets for Highly Sensitive Detection of mucin 1: Consistency between Electrochemical and Surface Plasmon Resonance Methods. *2D Mater.* **2017**, *4*, 025098.
(37) Zhu, Q.-Q.; Zhang, H.-W.; Yuan, R.; He, H. Ingenious Fabrication of Metal−Organic Framework/Graphene Oxide Composites as Aptasensors with Superior Electrochemical Recognition Capability. *J. Mater. Chem. C* **2020**, *8*, 15823−15829.
(38) He, H.; Wang, S.-Q.; Han, Z.-Y.; Tian, X.-H.; Zhang, W.-W.; Li, C.-P.; Du, M. Construction of Electrochemical Aptasensors with Ag(I) Metal−Organic Frameworks toward High-Efficient Detection of Ultra-Trace Penicillin. *Appl. Surf. Sci.* **2020**, *531*, 147342.
(39) Zhang, H.-W.; Zhu, Q.-Q.; Yuan, R.; He, H. Crystal Engineering of MOF@COF Core-Shell Composites for Ultra-

https://doi.org/10.1021/acs.inorgchem.1c00952
Inorg. Chem. 2021, 60, 11081−11089

Sensitively Electrochemical Detection. *Sens. Actuators, B* **2021**, *329*, 129144.
(40) Ebrahimi Vafaye, S.; Rahman, A.; Safaeian, S.; Adabi, M. An Electrochemical Aptasensor Based on Electrospun Carbon Nanofiber Mat and Gold Nanoparticles for the Sensitive Detection of Penicillin in Milk. *J. Food Meas. Charact.* **2021**, *15*, 876−882.
(41) Sheldrick, G. M. *SADABS, Program for Empirical Absorption Correction for Area Detector Data*; University of Gottingen: Gottingen, Germany, 1996.
(42) Sheldrick, G. M. Phase Annealing in *SHELX-90*: Direct Methods for Larger Structures. *Acta Crystallogr., Sect. A: Found. Crystallogr.* **1990**, *46*, 467−473.
(43) Sheldrick, G. M. A Short History of *SHELX*. *Acta Crystallogr., Sect. A: Found. Crystallogr.* **2008**, *64*, 112−122.
(44) Sheldrick, G. M. Crystal Structure Refinement with *SHELXL*. *Acta Crystallogr., Sect. C: Struct. Chem.* **2015**, *71*, 3−8.
(45) Dolomanov, O. V.; Bourhis, L. J.; Gildea, R. J.; Howard, J. A. K.; Puschmann, H. *OLEX2*: A Complete Structure Solution, Refinement and Analysis Program. *J. Appl. Crystallogr.* **2009**, *42*, 339−341.
(46) Zhang, L.-Y.; Liu, G.-F.; Zheng, S.-L.; Ye, B.-H.; Zhang, X.-M.; Chen, X.-M. Helical Ribbons of Cadmium(II) and Zinc(II) Dicarboxylates with Bipyridyl−Like Chelates−Syntheses, Crystal Structures and Photoluminescence. *Eur. J. Inorg. Chem.* **2003**, *2003*, 2965−2971.
(47) Yuan, R.; Yan, Z.; Shaga, A.; He, H. Design and Fabrication of an Electrochemical Sensing Platform Based on a Porous Organic Polymer for Ultrasensitive Ampicillin Detection. *Sens. Actuators, B* **2021**, *327*, 128949.
(48) Han, Z.-Y.; Zhu, Q.-Q.; Zhang, H.-W.; Yuan, R.; He, H. A Porous Organic Framework Composite Embedded with Au Nanoparticles: An Ultrasensitive Electrochemical Aptasensor toward Detection of Oxytetracycline. *J. Mater. Chem. C* **2020**, *8*, 14075−14082.
(49) Zhao, J.; Guo, W.; Pei, M.; Ding, F. GR−Fe_3O_4 NPs and PEDOT−AuNPs Composite based Electrochemical Aptasensor for the Sensitive Detection of Penicillin. *Anal. Methods* **2016**, *8*, 4391−4397.
(50) El-Shahat, M. F.; Burham, N.; Abdel Azeem, S. M. Flow Injection Analysis−Solid Phase Extraction (FIA−SPE) Method for Preconcentration and Determination of Trace Amounts of Penicillins using Methylene Blue Grafted Polyurethane Foam. *J. Hazard. Mater.* **2010**, *177*, 1054−1060.
(51) EL-Zahry, M. R.; Refaat, I. H.; Mohamed, H. A.; Rosenberg, E.; Lendl, B. Utility of Surface Enhanced Raman Spectroscopy (SERS) for Elucidation and Simultaneous Determination of Some Penicillins and Penicilloic Acid using Hydroxylamine Silver Nanoparticles. *Talanta* **2015**, *144*, 710−716.
(52) Hsieh, S.-H.; Huang, H.-Y.; Lee, S. Determination of Eight Penicillin Antibiotics in Pharmaceuticals, Milk and Porcine Tissues by Nano-Liquid Chromatography. *J. Chromatogr. A* **2009**, *1216*, 7186−7194.
(53) Pennacchio, A.; Varriale, A.; Scala, A.; Marzullo, V. M.; Staiano, M.; D'Auria, S. A Novel Fluorescence Polarization Assay for Determination of Penicillin G in Milk. *Food Chem.* **2016**, *190*, 381−385.
(54) Han, Z.-Y.; Zhang, H.; Li, H.-K.; Zhu, Q.-Q.; He, H. Ingenious Construction of an Electrochemical Aptasensor Based on a Au@COF/GO-NH_2 Composite with Excellent Detection Performance. *J. Mater. Chem. C* **2021**, *9*, 4576−4582.

https://doi.org/10.1021/acs.inorgchem.1c00952
Inorg. Chem. 2021, 60, 11081−11089